Solid Freeform Fabrication 2024: Proceedings of the 35th Annual International Solid Freeform Fabrication Symposium – An Additive Manufacturing Conference
Reviewed Paper

Mechanical and corrosion properties of stainless steel fabricated by wire arc additive manufacturing (WAAM) using weave and stringer beads

Stevens G. Hill Jr. [1*], Jared D. Seals [1], Mohammadamin Ezazi [1], Hossein Taheri [2], Bishal Silwal [1*],

[1] *Department of Mechanical Engineering, Georgia Southern University, Statesboro, GA, USA 30458*

[2] *Department of Manufacturing Engineering, Georgia Southern University, Statesboro, GA, USA 30458*

** Corresponding Authors: sh10931@georgiasouthern.edu; bsilwal@georgiasouthern.edu*

ABSTRACT

Wire-Arc-Additive-Manufacturing shows promise as a manufacturing method for large structures. However, careful control of material properties is required due to the number of process variables involved. Traditional welding techniques employ many different weaving methods to produce various bead properties in different situations. The effect of these weave patterns on the porosity and tensile strength of the produced prints is studied to determine if a relationship exists been print weave settings and the quality of printed samples. Walls which have been manufactured using Wire-Arc-Additive-Manufacturing are analyzed using non-destructive ultrasonic testing to quantify sample porosity. Microhardness testing is performed to define the heat affected zones. Corrosion analysis is performed on sample slices to understand the effect on corrosion resistance. Similar, adjacent sample slices underwent tension testing to determine if the yield point of the samples is affected by weave conditions.

INTRODUCTION

Additive manufacturing has seen a significant increase in industry interest. However, significant difficulties still arise when large scale metal additive manufacturing is required. These parts are frequently far too large for the scale of most powder-based or other directed energy deposition systems. In these instances, a different technique suited to large scale parts is needed. Specifically, a process which allows high deposition rates relative to conventional processes could result in a significant reduction in component lead time and cost, which is highly attractive in a production environment. In these cases, wire-arc-additive-manufacturing (WAAM) can be an alternative solution to the size, cost, and production speed limitations of traditional additive manufacturing methods. [1] [3] [4].

Wire-arc-additive-manufacturing is a large-scale additive manufacturing process which occurs using a variety of welding processes including GMAW (Gas-Metal-Arc-Welding), GTAW (Gas-Tungsten-Arc-Welding), or PAW (Plasma-Arc-Welding) [6]. Using the selected process, layer-based material deposition is controlled using an industrial 6DOF robot arm. The desired print geometry is “sliced” into 2D geometries or layers. These 2D geometries can then be used for robot programming. Process variables are adjusted through weld settings within the weld power supply. WAAM is exceptionally well suited to thin-walled geometries which can be easily replicated using successive passes of narrow, equidistant beads. When the path of the robot while printing these beads is parallel, each individual bead is programmed as a straight line. These narrow, straight welds are known “stringer” welds. Geometries which can be broken down into

series of stringer welds are easily produced using WAAM. However, frequently a part must be printed which has varying wall thickness throughout the geometry. In these scenarios, a hybrid weaving/stringer path, or a weaving path of varying weave amplitude could allow printing of thicker sections of the geometry in fewer passes [10], or even a single pass [13]. This practice can only be viable if the properties of the material printed in the stringer and weaving paths exhibit similar properties [11].

Stainless Steel 316L is of particular interest due to its high resistance to corrosion. It is widely used in the automotive and aerospace industries where the need for reduced weight is likely to continue to foster designs which are based on additive manufacturing. This steel (316L, AWS A5.9) is a low-carbon, austenitic stainless steel which has more Molybdenum than conventional stainless steel 316 resulting in improved corrosion resistance [2]. Significant research has been performed regarding the corrosive and microstructural properties of 316L manufactured through WAAM [7][8]; however, further investigation is required to determine if the corrosion, microstructure, and strength properties are affected by weaving, and if so whether these properties are detrimental to the intended function of the material.

MATERIALS AND METHODS

1. *Robot Path Programming*

Conventional welding incorporates multiple different welding strategies to obtain optimal mechanical properties depending on the welding application. These different strategies often involve weaving patterns that can be chosen based on operator skill or mechanical needs. For WAAM it is usual for the welding paths to be composed of stringer sections due to the relatively large areas that need to be filled. This stringer pathing method allows for higher deposition rates and increased layer heights; thus, they are optimal for use in taller structures and rapid production. As previously stated, weaving methods can lead to increased mechanical properties for conventional joint welding as well as effective fill for solid geometries, because of this a standard triangular weaving method was chosen as a comparative method to the stringer method used for WAAM.

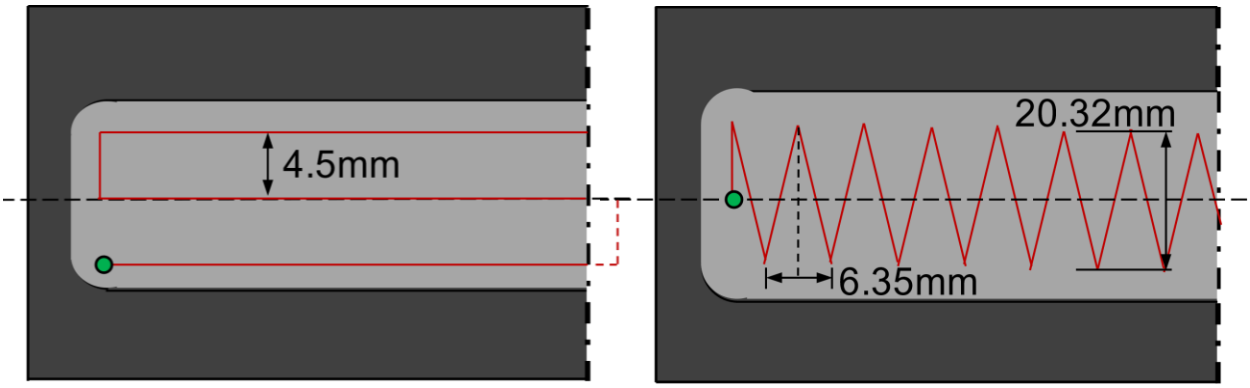

Figure 1. *Straight Stringer (Left) and Zigzag Weave (Right) WAAM Path Profiles*
(outer perimeter signifies substrate geometry for scale)

To compare the welding methods, two different wall structure paths had to be programmed

with differing welding parameters. The stringer wall program was pathed with the conventional straight stringer method as seen in Fig. 1. This pathing was a continuous weld with three main weld beads that traversed the entire length of the wall geometry (279.4mm) with smaller connecting beads (4.5mm) to maintain arc between welds and prevent collapsing (cratering) of end geometry. For this same reason, the path is “flipped” after every layer so that the start and stop points do not overlap. The zigzag weave program occurred in a similar manner using the programming suite within the KRC (Kuka Robot Controller) pendant. The final path shape for a single layer resembled a ‘Z’ shape. This programming also “flipped” after every layer to avoid cratering, or a defect caused by the high heat during arc initialization. “Flipping” refers to rotating the weld path 180^{o} about its transverse and longitudinal axes. “Flipping” prevents the starts and stops of subsequent layers from aligning vertically which could cause inconsistencies in height of the final geometry. Weld parameters were selected based on researcher’s knowledge from prior testing. These parameters are listed in Table 1 below.

Table 1. Summary of Experiment Parameters

	Setting	Stringer Profile	Weave Profile
WAAM Process Parameters	Voltage (V)	28.65	28.65
	Current (A)	375	375
	Feed Rate (mm/s)	158.75	158.75
	Travel Speed (mm/s)	12.70	4.20
	Layer Offset (mm)	2.30	1.60
	Layer Count	15	20
	Cooldown (sec)	30	30
	Bead Offset (mm)	4.5	----------
Weave Parameters	Weave Pattern	----------	Triangle
	Length (mm)	----------	6.35
	Deflection (mm)	----------	10.16
	Angle (degrees)	----------	0

The triangular (zigzag) pathing was based on centerline along the substrate with a deflection of 10.16mm in either direction from the centerline and a travel distance of 6.35mm per full oscillation. (Fig. 1) In total this required 44 periods to traverse the entire length of the wall geometry. Much like the stringer wall, there was a need to alternate the starting and stopping positions of each layer of the wall. To accomplish this, stopping points would alternate between each of the layers. The layer height offset for the weave pathing had been previously found to be 1.6mm per layer with a lower deposition rate than the stringer pathing of 4.2 mm/s. This lower deposition rate was attributed to the increased overall distance of the pathing for each layer of the weave wall.

2. *WAAM of 316L Weaving and Non-Weaving Walls*

WAAM occurs using a commercially available Kuka KR 6 industrial robot paired with a Lincoln Electric R450 power supply and torch, using Radnor 316L welding wire for deposition. Pulsed spray deposition is utilized to increase the deposition rate and effectively lower thermal input. An Argon (90%), Carbon-Dioxide (8%), and Oxygen (2%) trimix shielding gas intended for stainless steels is supplied at a rate of 35 L/h. A standard wall geometry is selected for sample analysis as this is a common measure used in the analysis of material properties produced by WAAM. One wall each was printed for the weaving and non-weaving weld trajectories. Deposition occurs on

an A36 steel build plate, and a small sacrificial layer (5mm) is not considered for testing to avoid possible elemental diffusion from the baseplate during thermal cycling. Each wall is printed with a three-bead width but requires different numbers of layers to reach the same print height. Observation showed weaving resulted in a large width increase (+36.8%, +2.22mm) and layer height decrease (-30.4%, -0.7mm) which can be partly attributed to the increased residence time of the weld pool during weaving, among other factors. Significantly increased bead height to width ratio has been reported through intensive in-situ cooling of straight line-bead geometries, and this would likely hold true for weaving profiles. [9]

3. *Sample Collection Methods*

After the walls have each been successfully printed, it is required that they are removed from the baseplate so that material samples can be created. This is performed by first removing one side of the baseplate from the remaining wall and baseplate using a plasma torch. This leaves only the printed wall and a small portion of the baseplate which does not protrude into the workspace of the waterjet. Tabs are then welded perpendicular to the bottom of the baseplate to allow clamping in the waterjet. Fixturing the wall in this way (Fig. 2-Left) maximizes the number of collectable samples in each print, in turn reducing the necessary print height for effective sample collection. The waterjet is then used to slice 5mm thick transverse samples from the wall, parallel to the baseplate, until too little material remains without risking possible intrusion from elemental diffusion (about 5mm). A small tab is left uncut to hold the slices together until they can be individually labeled, and the orientation and position of each sample recorded. These 5mm thick rectangular samples are then halved, to again increase the number of material samples in each wall (Fig. 2-Right). Deburring is the final step before first performing non-destructive testing techniques, and eventually destructive techniques.

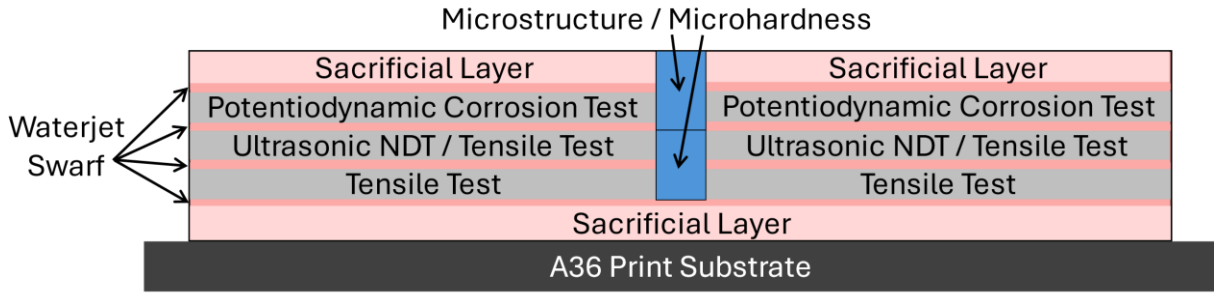

Figure 2. (Top) Waterjet Slicing of Printed Wall; (Bottom) Sample Collection Diagram

RESULTS AND DISCUSSION

1. Corrosion Analysis

Corrosion tests were performed in saline water (3.5 wt.% sodium chloride in deionized water) using a three-electrode electrochemical setup and by employing the potentiodynamic polarization method. The electrodes included Ag/AgCl as the reference electrode, graphite rod as the counter electrode, and the 316L Steel sample as the working electrode. The Tafel plots were scanned using the following parameters:

Table 2. Summary of Tafel Plot Parameters

Initial E(V)	Final E(V)	Scan Rate (mV/s)	Sample Period (s)	Density (g/cm^2)	Equivalent Weight	Initial Delay (s)	Stab (mV/s)	Area of Sample Submerged (cm^2)
-0.25 vs Eoc	0.25 vs Eoc	10	1	7.87	28.25	600	0.1	4

Figure 3 shows the measured Tafel plots for 316L Steel samples and Table 2 summarizes the values of corrosion current density (I_{corr}) and corrosion potential (E_{corr}).

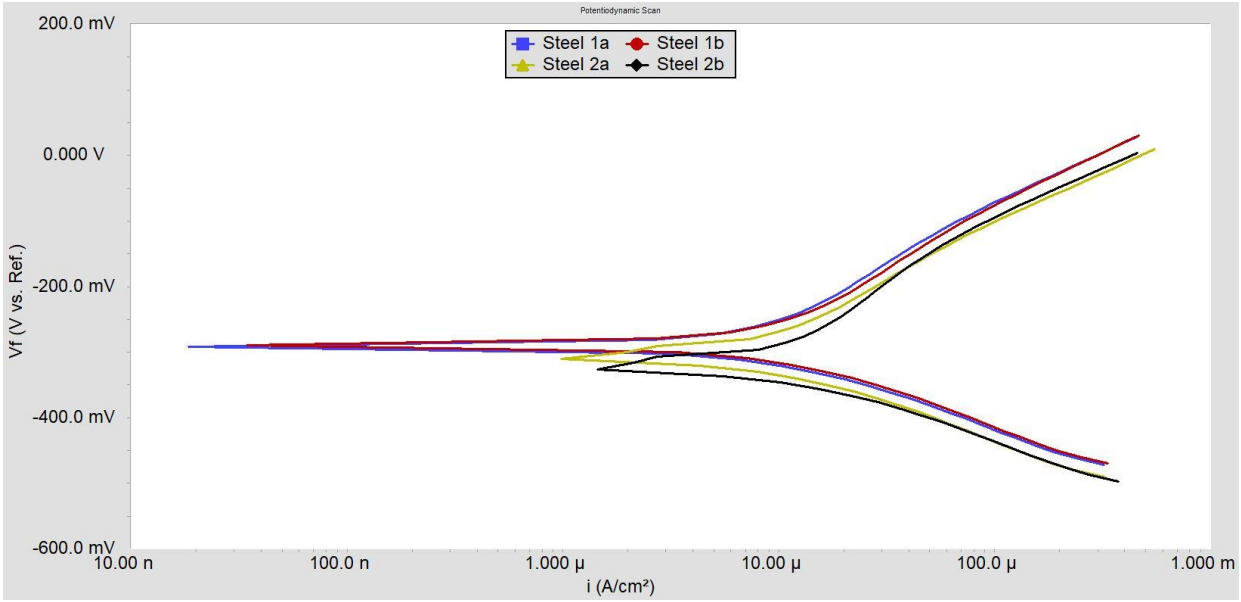

Figure 3. Tafel plots for 316L Steel samples.

Table 3. Summary of corrosion current density (I_{corr}) and corrosion potential (E_{corr}) values for 316L Steel samples.

316L Steel samples	**I_{corr} (µA/cm^2)**	**E_{corr} (mV)**
With Weave (Sample 1A)	10.5	-292
With Weave (Sample 1B)	11.5	-290
Without Weave (Sample 2A)	9.33	-306
Without Weave (Sample 2B)	11.3	-321

According to the electrochemical kinetics of corrosion [5] [14], a more positive value of E_{corr} indicates a lower corrosion probability, while I_{corr} is a measure of the corrosion rate. Therefore, it can be inferred that Sample 2A, with the lowest I_{corr} value of 9.33 µA/cm^2 shows the highest protection against corrosion (lowest susceptibility), whereas Sample 1B, with an I_{corr} value of 11.5 µA/cm^2, demonstrates the lowest corrosion protection (highest susceptibility).

2. *Microstructure Overview*

The microstructures of the two samples are different mainly due to the differing pathing methods. The weave pathing allowed for more cooling time for each layer, as the deposition for each layer took an increased amount of time when compared to the stringer pathing. This increased cooling time between each layer produced abrupt microstructure changes between each of the stratified layers (Fig. 4). Unlike the weave pathing microstructure, the stringer microstructure had arrays of bead outlines rather than stratified layers. Just by looking at the grain boundaries, the beads that make up each of the layers for the stringer and weave methods are noticeable and the overlapping fusion zones can be seen.

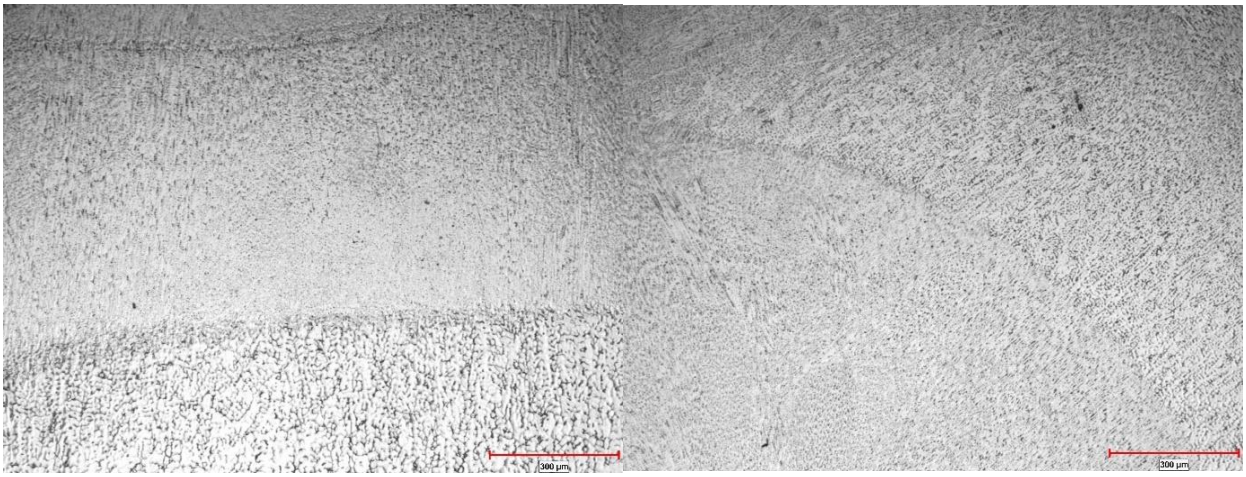

Figure 4. (Left) 5X Weave Pathing Microstructure, (Right) 5X Stringer Pathing Microstructure [300µm scale]

3. Non-Destructive Ultrasonic Evaluation

Ultrasonic nondestructive testing (NDT) in the form of immersion method was used to assess the integrity of the parts. Fig 5. Shows the experimental setup where a 10 MHz flat surface immersion transducer (Dia. = 0.5") was placed at 100 mm distance above the part top surface. Scanning was performed on the area of 280 mm x 60 mm (X, Y) with scan-step and index step both equal to 1 mm and scanning speed of 20 mm/sec.

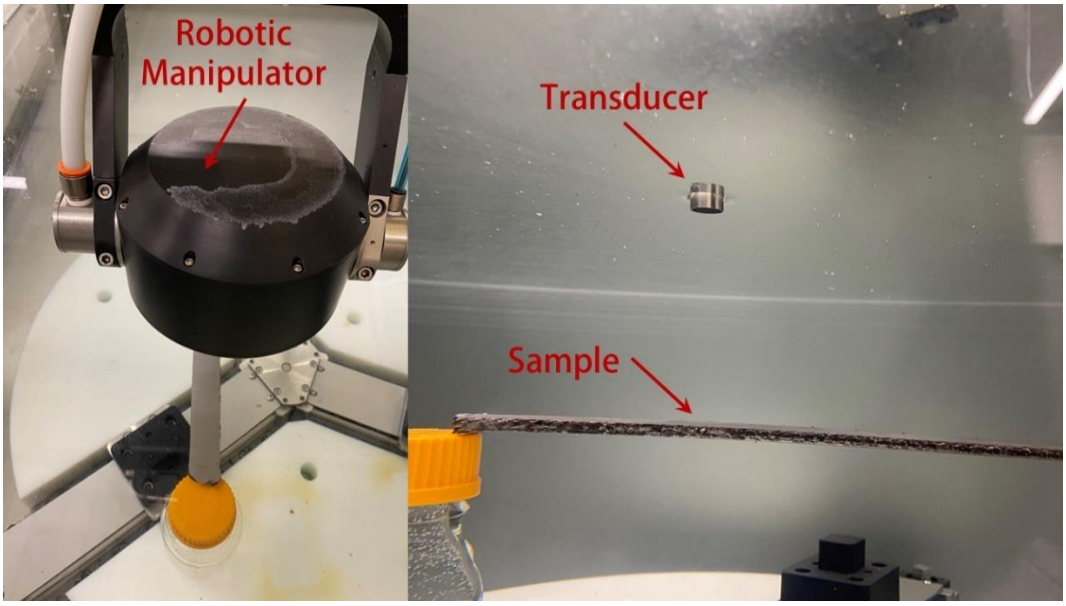

Figure 5. Immersion ultrasonic NDT experimental setup

Ultrasonic NDT results in form of A-scan, B-scan, and C-scans for both weaving and non-weaving parts are presented in Figures 6 and 7. For both parts, the regions with the higher concentration of voids are visible as high-amplitude indicators. For the weaving part, most of these indicators are in the top-right side of the image. In addition, a linear pattern of high-amplitude indicators is visible in the lower side of the sample. The curser locator in Figure 6 indicates one

of the largest indicators which is also visible in B-scans images (Top-Left and Bottom-Right graphs in the image).

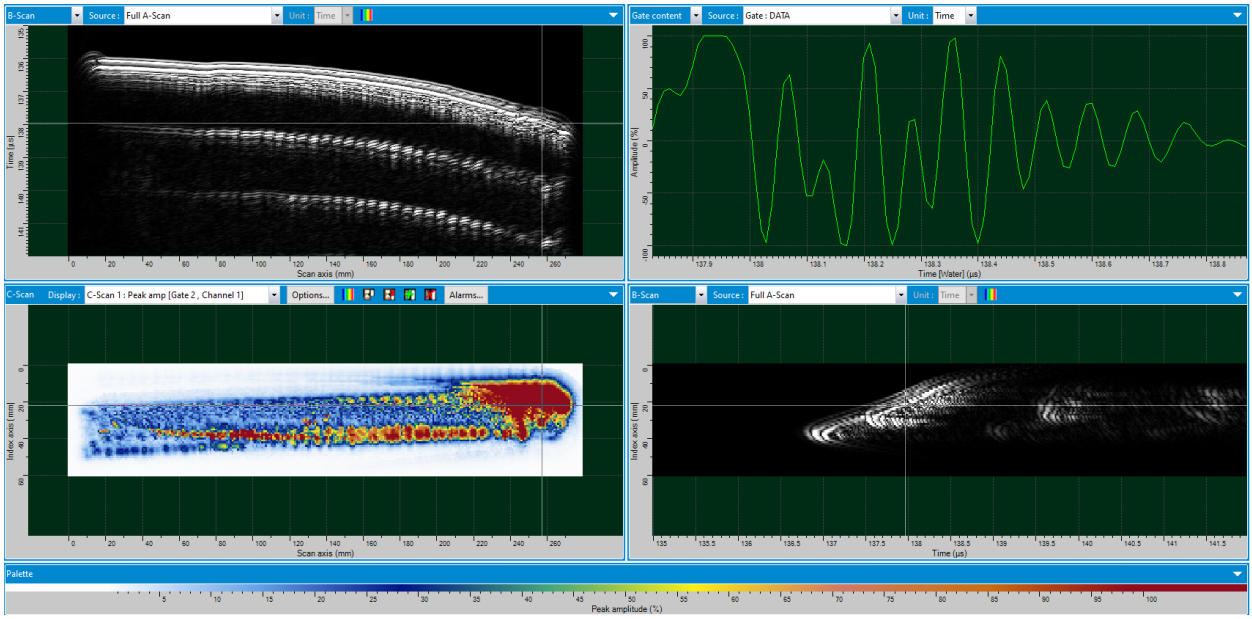

Figure 6. Ultrasonic NDT results in form of A-scan (Top-Right), B-scans (Top-Left and Bottom-Right), and C-scan (Bottom-Left) for weaving part

In the non-weaving part, the indicators have a wider distribution almost all over the sample. The distribution of indicators all over the sample indicates the higher overall pore distribution in non-weaving part compared to the weaving part. The curser locator in Figure 7 indicates one of the largest indicators in lower side linear cluster of indications which is also visible in B-scans images (Top-Left and Bottom-Right graphs in the image). The location and concentration of pores is of importance as pores can provide failure planes within the material and can result in crack propagation between adjacent pores.

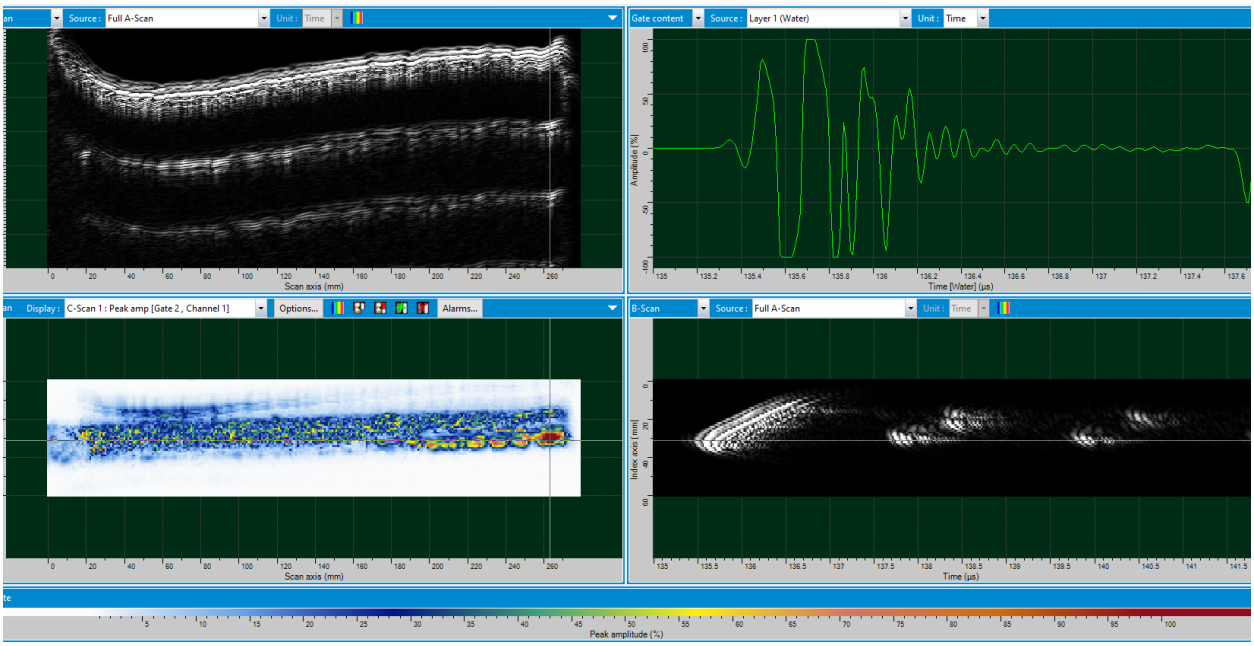

Figure 7. Ultrasonic NDT results in form of A-scan (Top-Right), B-scans (Top-Left and Bottom-Right), and C-scan (Bottom-Left) for non-weaving part

4. Microhardness Evaluation

Microhardness measurements were carried out on two equally sized samples from similar locations in each of the 316L wall depositions. The samples were oriented in the direction of deposition and the hardness measurements were taken along the centerline at 0.5mm increments, starting from the top of each sample. All the microhardness tests were conducted with a 500gf load and a 10-second dwell time. With an expected layer height of 2.3mm for the stinger wall and 1.6mm for the weave wall, this allowed for three to four microhardness tests per deposition layer. This test density allowed for the determination of the microhardness gradient throughout each of the layers of each of the wall depositions (Fig. 8). The offset of the data is caused by the first few millimeters of the print being considered sacrificial due to elemental diffusion near the substrate boundary.

The 316L weave deposition showed a pattern of overall hardening as the distance from the substrate increased until the top few layers of the wall. The weave deposition had an average hardness value of 226.6 HV, with the highest hardnesses located at 23.5mm and 19.5mm from the substrate. The stringer deposition showed an overall consistent hardness throughout the wall except for the lowest tested layers and the uppermost tested layers. Both areas had increased hardness relative to the rest of the sample. Overall, the stringer wall had an average hardness of 219.9 HV and a maximum hardness value at 8mm from the substrate.

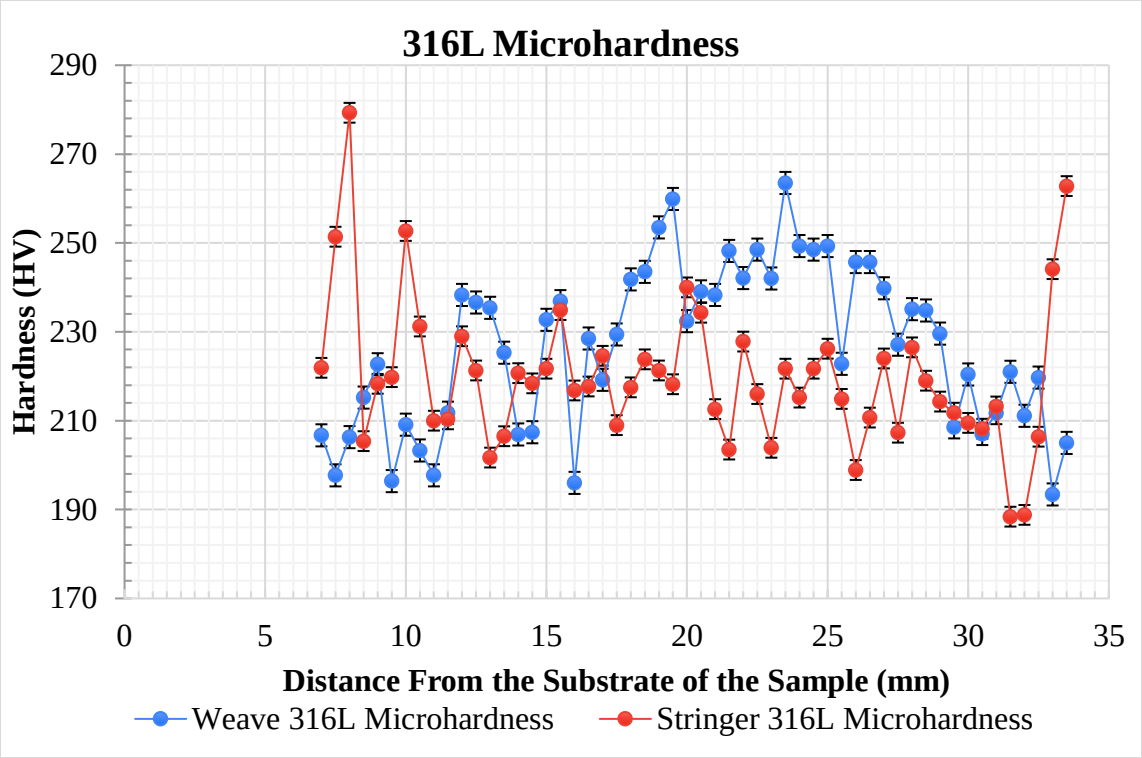

Figure 8. Microhardness Plot of 316L String and Weave Samples

5. *Tensile Testing*

Tensile testing occurred using an MTS 250kN tensile frame with hydraulic wedge grips. Tensile samples were produced using 5mm “slices” of the stringer and weaving walls at similar locations. Fig. X displays the stress-strain plot produced through testing of both samples. In the elastic region, the samples exhibit similar linear relationships between stress and strain as expected. Upon approaching yielding, the sample produced using weaving begins to yield at a lower stress. The samples reach their yield point and plastic deformation begins. In the plastic region, both samples retain similar slopes until necking begins. Neither failure nor noticeable necking occurred during testing of the stringer sample. Testing was concluded at a strain of 0.5. The weaving sample began to neck, effectively flattening the curve, near a strain of 0.37. Post test observations revealed that failure likely occurred due to a combination of surface defects and print direction. In the stringer sample, the deposition direction is parallel to the test direction. This means that shear stresses are negligible at the interface between subsequent beads. However, in the weaving specimen shear forces could exist at the inter-bead boundary.

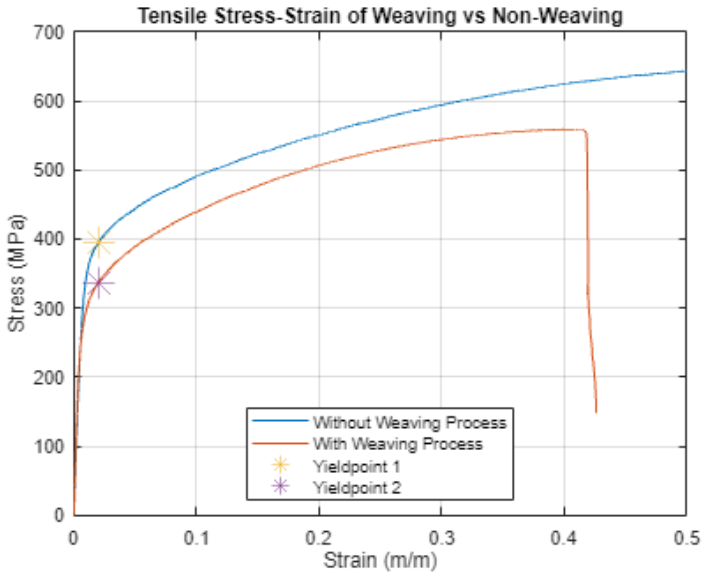

Figure 9. Stress-Strain Plot of WAAM 316L Tensile Samples

Upon examination of the stress-strain curve, the stringer sample performed well under tension resulting in a Modulus of Elasticity that is 5.1% better when compared with the weaving sample (Table 4). The produced stress strain plots are in good agreement with the room temperature testing conducted by [12] While failure was not reached at the test end parameter of 0.5 strain, some 316L samples produced through GMAW WAAM reported to fail at elongations >60% in some orientations. [12].

Table 4. Strength Properties of WAAM 316L Tensile Samples

	Labels	Yield Point (MPa)	Modulus of Elasticity (GPa)
1	Without Weaving Process	394.87	44.75
2	With Weaving Process	337.13	42.59

CONCLUSION

Wire-Arc-Additive-Manufacturing has gained significant interest due to its ability to provide large-format accurate prints. However, when complex geometries are involved, weaving may be required. Two sample walls were produced using stringer and zigzag weave patterns. From these walls samples were produced and evaluated using 316l wire feedstock. From this evaluation, following conclusion can be made:

1. Corrosion testing showed that the weaving sample was slightly less likely to corrode; however, corrosion would occur at a faster rate once it has begun.
2. Non-destructive evaluation showed that the stringer part has higher distribution of pores.
3. Microstructure evaluation revealed that the different thermal cycles in each wall resulted in different microstructures, with stratified layers present in the weave sample. Larger
4. The weaving sample was also harder and more scatter during microhardness evaluation.
5. Finally, tensile testing and the stress-strain plots produced reveal that the weaving process did result in a slightly lower yield point.

REFERENCES

[1] Bekker, Anne C.M., et al. “CHALLENGES IN ASSESSING THE SUSTAINABILITY OF WIRE + ARC ADDITIVE MANUFACTURING FOR LARGE STRUCTURES.” *Solid Freeform Fabrication Symposium*, 2016.

[2] Collins, Garrett C., "The Effects of Weave Patterns in Wire Arc Additive Manufacturing Using 316L Stainless Steel" (2024). Honors College Theses. 996. https://digitalcommons.georgiasouthern.edu/honors-theses/996

[3] Cunningham, C.R., et al. “Cost modelling and sensitivity analysis of wire and arc additive manufacturing.” *Procedia Manufacturing*, vol. 11, 2017, pp. 650–657, https://doi.org/10.1016/j.promfg.2017.07.163.

[4] Dias, Manuel, et al. “Economic and environmental potential of wire-arc additive manufacturing.” *Sustainability*, vol. 14, no. 9, 25 Apr. 2022, p. 5197, https://doi.org/10.3390/su14095197.

[5] Ezazi, Mohammadamin, et al. "Self-healable superomniphobic surfaces for corrosion protection." ACS applied materials & interfaces 11.33 (2019): 30240-30246.

[6] Jafari, D., Vaneker, T. H. J., & Gibson, I. Wire and arc additive manufacturing: Opportunities and challenges to control the quality and accuracy of manufactured parts. *Materials and Design*, *202*, 2021, https://doi.org/10.1016/j.matdes.2021.109471

[7] Karpagaraj, A., et al. “A review on the suitability of Wire Arc additive manufacturing (WAAM) for stainless steel 316.” *ADVANCES IN MECHANICAL DESIGN, MATERIALS AND MANUFACTURE: Proceeding of the Second International Conference on Design, Materials and Manufacture (ICDEM 2019)*, 2020, https://doi.org/10.1063/5.0004148.

[8] Ko, Gyeongbin, et al. “The corrosion of stainless steel made by Additive Manufacturing: A Review.” *Metals*, vol. 11, no. 3, 21 Mar. 2021, p. 516, https://doi.org/10.3390/met11030516.

[9] Li, F., Chen, S., Shi, J., Zhao, Y., & Tian, H. Thermoelectric cooling-aided bead geometry regulation in wire and arc-based additive manufacturing of thin-walled structures. *Applied Sciences (Switzerland)*, *8*(2), 2018. https://doi.org/10.3390/app8020207

[10] Ma, G., Zhao, G., Li, Z., & Xiao, W. A Path Planning Method for Robotic Wire and Arc Additive Manufacturing of Thin-Walled Structures with Varying Thickness. *IOP Conference Series: Materials Science and Engineering*, *470*(1), 2019. https://doi.org/10.1088/1757-899X/470/1/012018

[11] Sasikumar, C., & Oyyaravelu, R. Mechanical properties and microstructure of SS 316 L created by WAAM based on GMAW. *Materials Today Communications*, *38, 2024*. https://doi.org/10.1016/j.mtcomm.2023.107807

[12] Tang, W., Giuliano, D., Martinez, O., Banerjee, K., Nycz, A., Gussev, M., Meyer, L., & Vaughan, D. (n.d.). 316L Stainless Steel Wire Arc Additive Manufacturing and Characterization for Potential SNF Canister Production. http://energy.gov/downloads/doe-

[13] Venturini, G., Montevecchi, F., Bandini, F., Scippa, A., & Campatelli, G. Feature based three axes computer aided manufacturing software for wire arc additive manufacturing dedicated to thin walled components. *Additive Manufacturing*, *22*, 643–657, 2018. https://doi.org/10.1016/j.addma.2018.06.013

[14] Zhan, Zhibing, et al. "Superhydrophobic Al surfaces with properties of anticorrosion and reparability." ACS omega 3.12 (2018): 17425-17429.